Joule

CellPress

Article

Reactivity-Guided Interface Design in Na Metal Solid-State Batteries

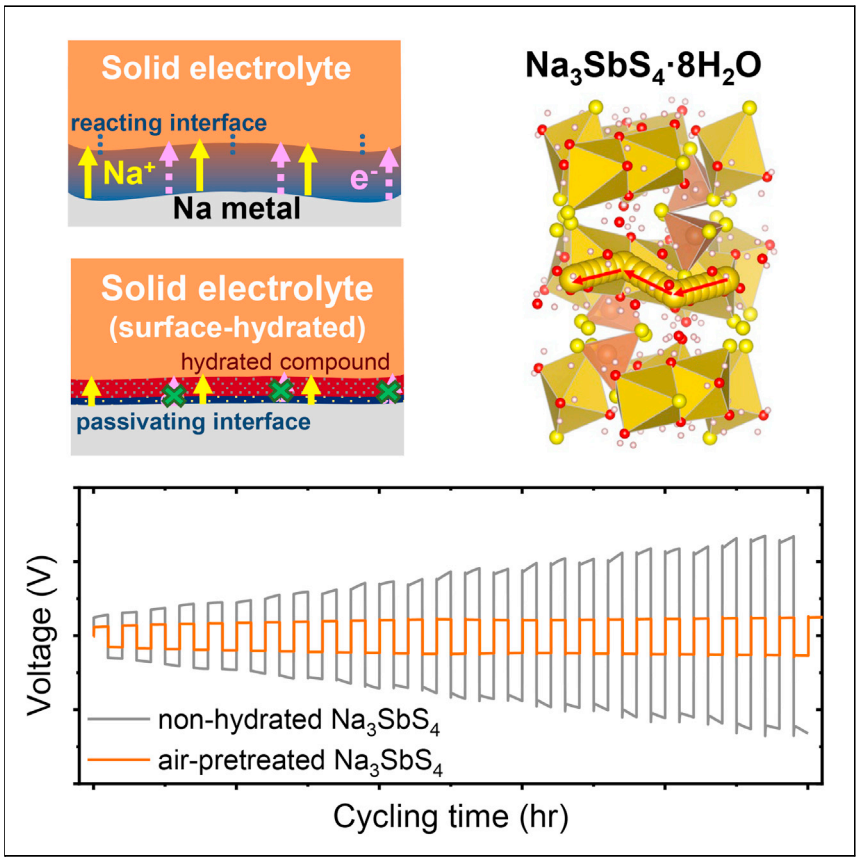

A key requirement for achieving high-energy density in solid-state batteries is highly efficient cycling of an alkali metal anode in a safe manner. Herein, we combine first-principles calculations and experimental characterizations to identify a protective hydrate coating for Na_3SbS_4 that leads to a passivating interface and greatly enhanced stability. The buried interface is characterized using *post-operando* synchrotron X-ray depth profiling. This finding identifies hydrates as promising for improving the metal/electrolyte interfacial stability and suggests a general strategy for interface design.

Yaosen Tian, Yingzhi Sun, Daniel C. Hannah, ..., Karena W. Chapman, Shou-Hang Bo, Gerbrand Ceder

shouhang.bo@sjtu.edu.cn (S.-H.B.)
gceder@berkeley.edu (G.C.)

HIGHLIGHTS

A passivating interface is reversely designed by first-principles computations

A hydrate coating for Na_3SbS_4 is identified for greatly enhanced stability

Non-destructive synchrotron XRD provides space-resolved interfacial information

Tian et al., Joule 3, 1–14
April 17, 2019
https://doi.org/10.1016/j.joule.2018.12.019

Please cite this article in press as: Tian et al., Reactivity-Guided Interface Design in Na Metal Solid-State Batteries, Joule (2019), https://doi.org/10.1016/j.joule.2018.12.019

Joule

CellPress

Article

Reactivity-Guided Interface Design in Na Metal Solid-State Batteries

Yaosen Tian,[1,2] Yingzhi Sun,[1,2] Daniel C. Hannah,[2] Yihan Xiao,[1,2] Hao Liu,[3] Karena W. Chapman,[3,4] Shou-Hang Bo,[2,5,*] and Gerbrand Ceder[1,2,6,*]

SUMMARY

Solid-state batteries provide substantially increased safety and improved energy density when energy-dense alkali metal anodes are applied. However, most solid-state electrolytes react with alkali metals, causing a continuous increase of the cell impedance. Here, we employ a reactivity-driven strategy to improve the interfacial stability between a Na_3SbS_4 solid-state electrolyte and sodium metal. First-principles calculations identify a protective hydrate coating for Na_3SbS_4 that leads to the generation of passivating decomposition products upon contact of the electrolyte with sodium metal. The formation of this protective coating, a newly discovered hydrated phase, is achieved experimentally through exposure of Na_3SbS_4 to air. The buried interface is characterized using *post-operando* synchrotron X-ray depth profiling, providing spatially resolved evidence of the multilayered phase distribution in the Na metal symmetric cell consistent with theoretical predictions. We identify hydrates as promising for improving the metal/electrolyte interfacial stability in solid-state batteries and suggest a general strategy of interface design for this purpose.

INTRODUCTION

The ability to create all-solid-state batteries is one of the most exciting prospects for energy storage.[1,2] Solid-state batteries have intrinsically higher safety, as the solid conductor replaces the flammable liquid electrolyte used in conventional lithium (Li)-ion and sodium (Na)-ion batteries. The development of inorganic solid-state electrolytes has been an active area of research, with multiple solids achieving ionic conductivities equaling or even surpassing those of their liquid counterparts. To date, various highly conductive inorganic solid conductors have been discovered, such as perovskite-type,[3] sodium superionic conductor (NASICON)-like,[4–6] garnet-type,[7–9] and sulfide-type materials.[10–19] In addition, general design principles have been developed to achieve high ionic mobility.[20]

It is now generally accepted that solid-state batteries will have to use metallic Li/Na anodes to be able to surpass traditional Li-ion cells in energy density.[21] This is particularly challenging as most solid-state electrolytes are reduced by alkali metals and form reaction layers that degrade rate capability and reduce capacity over time.[21–25] For instance, the cathodic decomposition of $Li_{10}GeP_2S_{12}$ (LGPS) is initiated by the reduction of Ge^{4+} and P^{5+} below 1.7 V versus Li/Li^+, forming $Li_{15}Ge_4$, Li_3P, and Li_2S.[23,26,27] Any reduction of metals in the conductor can create electronically conducting pathways, which lead to further growth of the decomposition layer. Only a few conductors are thermodynamically stable against Li metal (e.g., Li_3N and Li_3OCl),[25] and their limited ionic conductivity and/or poor oxidation stability limit their use in real batteries. While various coating and deposition methods have been developed to improve the wetting and/or chemical

Context & Scale

In solid-state batteries, the flammable liquid electrolyte conventionally used in Li or Na-ion batteries is replaced with an inorganic solid-state electrolyte, leading to substantially increased safety and, in principle, improved energy density, when energy-dense Li and Na anodes are applied in these systems. While various superionic conductors have been discovered, the integration of the conductors with Li or Na metals remains challenging, as most solid-state electrolytes are reduced by the alkali metals and form reaction layers that degrade electrochemical performance. In this work, we report a strategy for building a passivating interface between solid-state electrolyte and Na metal anode and improve this interfacial stability. Unlike other extrinsic barrier layers, such "built-in" passivating interface can reform whenever it is damaged or a new metal interface is formed, which occurs inevitably when an alkali metal deposits back on the anode in the charge cycle of the battery.

Please cite this article in press as: Tian et al., Reactivity-Guided Interface Design in Na Metal Solid-State Batteries, Joule (2019), https://doi.org/10.1016/j.joule.2018.12.019

stability between garnet oxide electrolyte and Li metal,[8,21,28] the high cost of these deposition methods makes it difficult to extend these methods to a wider range of solid-state electrolytes. Such barrier layer options are also less reliable for a strongly reacting interface such as the Na metal-sulfide electrolyte interface, where the large and inhomogeneous displacement of the electrode-electrolyte interface during cycling will jeopardize the mechanical integrity of the barrier layer. What is required is the formation of a passivating layer formed by the reaction of the conductor with the alkali metal anode that, unlike extrinsic barrier layers, can reform whenever the passivation layer is damaged or new metal interface is formed in contact with the conductor. This passivation mechanism would be able to protect the new interface that inevitably forms when an alkali metal deposits back on the anode in the charge cycle of the battery.

A passivating interface can be engineered by introducing selected elements and/or compounds that react beneficially with Li/Na metals, forming electronically insulating but ionically permeable decomposition products.[22,29–31] Similar concepts of extending the electrochemical stability window of solid-state electrolytes by forming passivating phases have been discussed in recent computational work.[23,25,26] Once the set of insulating solids that are stable against the alkali are identified, using, for example, high-throughput first-principles computational tools,[15,22,25] a solid-state conductor should be designed that will decompose to these insulating solids when in contact with the metal, leading to intrinsic passivation.

In this paper, we implement this reverse design strategy to improve the stability of a highly reacting Na/Na_3SbS_4 interface.[32,33] This is achieved through the formation of a hydrated layer on the surface of Na_3SbS_4. Hydration forms a novel phase ($Na_3SbS_4 \cdot 8H_2O$) with reasonable Na-ion conductivity on the surface of Na_3SbS_4. This hydrated phase partially reacts with Na metal, forming NaH and Na_2O as passivating products, which limit further decomposition of the solid-state electrolyte and reduce impedance growth upon cycling. *Post-operando* synchrotron X-ray depth profiling (SXDP), a non-destructive technique for probing the interface, was used to confirm that NaH and Na_2O were products of $Na_3SbS_4 \cdot 8H_2O$ in contact with metallic Na after the Na plating/stripping processes.

To further investigate the potential of this approach, we evaluated the decomposition products of all the Li and Na hydrate compounds present in the Materials Project[34] database against Li or Na metal, identifying hydrates as a promising class of materials for electrolyte protection. In addition, we further extend the strategy of interface reverse design and discuss the possible pretreatment of solid-state electrolytes with other chemicals besides water. Finally, we highlight the critical need to spatially resolve interfacial decomposition products in solid-state batteries, suggesting depth profiling and tomography as valuable characterization tools.

RESULTS

Reverse Design and Stability of Na/Na_3SbS_4 Interface

Using the first-principles methodology developed previously,[22,25] the decomposition products of a conductor can be predicted under different Li or Na chemical potentials. Taking Na_3SbS_4, a recently reported superionic Na conductor,[19,33] and Na metal as an example, the most thermodynamically favorable reactions (if any) occurring between the Na-ion conductor and Na metal reservoir is calculated to be

$$8\ Na + Na_3SbS_4 \rightarrow 4\ Na_2S + Na_3Sb. \qquad \text{(Reaction 1)}$$

The predicted decomposition products of Na_3SbS_4 over the full range of Na chemical potentials are listed in Table S1. The large fraction of metallic Na_3Sb in

[1]Department of Materials Science and Engineering, University of California, Berkeley, Berkeley, CA 94720, USA

[2]Materials Sciences Division, Lawrence Berkeley National Laboratory, Berkeley, CA 94720, USA

[3]Materials Science Division and X-ray Science Division, Advanced Photon Source, Argonne National Laboratory, Argonne, IL 60439, USA

[4]Department of Chemistry, Stony Brook University, Stony Brook, NY 11794, USA

[5]University of Michigan, Shanghai Jiao Tong University Joint Institute, Shanghai Jiao Tong University, Minhang District, Shanghai 200240, P.R. China

[6]Lead Contact

*Correspondence: shouhang.bo@sjtu.edu.cn (S.-H.B.), gceder@berkeley.edu (G.C.)

https://doi.org/10.1016/j.joule.2018.12.019

Please cite this article in press as: Tian et al., Reactivity-Guided Interface Design in Na Metal Solid-State Batteries, Joule (2019), https://doi.org/10.1016/j.joule.2018.12.019

Reaction 1 in the decomposition products indicates the likely formation of a percolating electronic conduction path at the interface. Therefore, continuous decomposition of bulk Na_3SbS_4 is expected to occur until either the Na metal or the Na_3SbS_4 solid-state electrolyte is completely consumed.

To evaluate the compatibility between Na_3SbS_4 and Na metal experimentally, a symmetric Na/Na_3SbS_4/Na cell was cycled at a constant current (0.1 mA cm^{-2}). The synthesis and characterization of Na_3SbS_4 are described in the Experimental Procedures and in Figures S1–S3. The results are fully consistent with the theoretical predictions discussed above. As shown in Figure 1A, the Na plating/stripping voltage continuously increases from an initial value of 0.13 V to 0.67 V after 25 h of cycling, suggesting increasing polarization due to the unstable Na/Na_3SbS_4 interface. Na_2S could be identified as one of the decomposition products after cycling of the symmetric cell using synchrotron X-ray diffraction (SXRD) performed at beam line 11-ID-B at the Advanced Photon Source (APS) at Argonne National Laboratory (Figure 1B), consistent with the theoretical prediction of Reaction 1. The same products as those predicted in Reaction 1 were also identified using X-ray photoelectron spectroscopy in Wu et al.[32] A digital photograph and scanning electron microscopy (SEM) images of the Na/Na_3SbS_4 interface after 25 cycles are presented in Figures S4 and S5.

Based on our previous first-principles screening results on the stability window of most Na-containing compounds, NaH and Na_2O are predicted to be thermodynamically stable upon contact with Na metal. Both compounds have been reported to exhibit high ionic conductivity and electronic resistivity,[35–37] making them desirable for interface passivation. To bring in the H and O needed to form NaH and Na_2O at the interface, Na_3SbS_4 was partially hydrated. As reported in the literature,[19,33] Na_3SbS_4 is stable in a dry air atmosphere, whereas a fully hydrated phase, $Na_3SbS_4 \cdot 9H_2O$, can be generated in the presence of moisture. The reactivity of $Na_3SbS_4 \cdot 9H_2O$ in contact with the Na reservoir was evaluated for the full range of Na chemical potentials, and the results are summarized in Table S2. The most favorable reaction at 0 V versus Na/Na^+ is determined to be

$$44\ Na + Na_3SbS_4 \cdot 9H_2O \rightarrow 4\ Na_2S + Na_3Sb + 18\ NaH + 9\ Na_2O. \quad \text{(Reaction 2)}$$

As shown in Reaction 2, Na_2O and NaH will be generated when $Na_3SbS_4 \cdot 9H_2O$ is in contact with Na metal. As opposed to the large fraction of Na_3Sb generated in Reaction 1, the fraction of the electron conducting phase is greatly decreased to 3 mol % in Reaction 2, which can result in substantially improved interface stability.

A symmetric cell using a surface-hydrated Na_3SbS_4 pellet as the solid-state electrolyte was constructed to experimentally examine the effect of electrolyte hydration on the stability of the Na/Na_3SbS_4 interface. The as-prepared Na_3SbS_4 pellet was exposed to ambient air at a humidity of approximately 68% for 10 min before being sandwiched in metallic Na foils. The cells were assembled using otherwise identical procedures, and Na_3SbS_4 from the same batch was used to maximize consistency. The changes in the surface morphology of the Na_3SbS_4 pellet during the hydration process can be observed in the SEM images presented in Figures 1C–1E. Figure 1F presents schematic illustrations of the Na metal/Na_3SbS_4 interface with and without the hydrated layer. As observed in Figure 1A, a substantially smaller voltage increase occurred after cycling for the surface-hydrated Na_3SbS_4 than for its non-hydrated counterpart, which indicates improved interfacial stability and effective protection provided by the hydrate protective layer.

Please cite this article in press as: Tian et al., Reactivity-Guided Interface Design in Na Metal Solid-State Batteries, Joule (2019), https://doi.org/10.1016/j.joule.2018.12.019

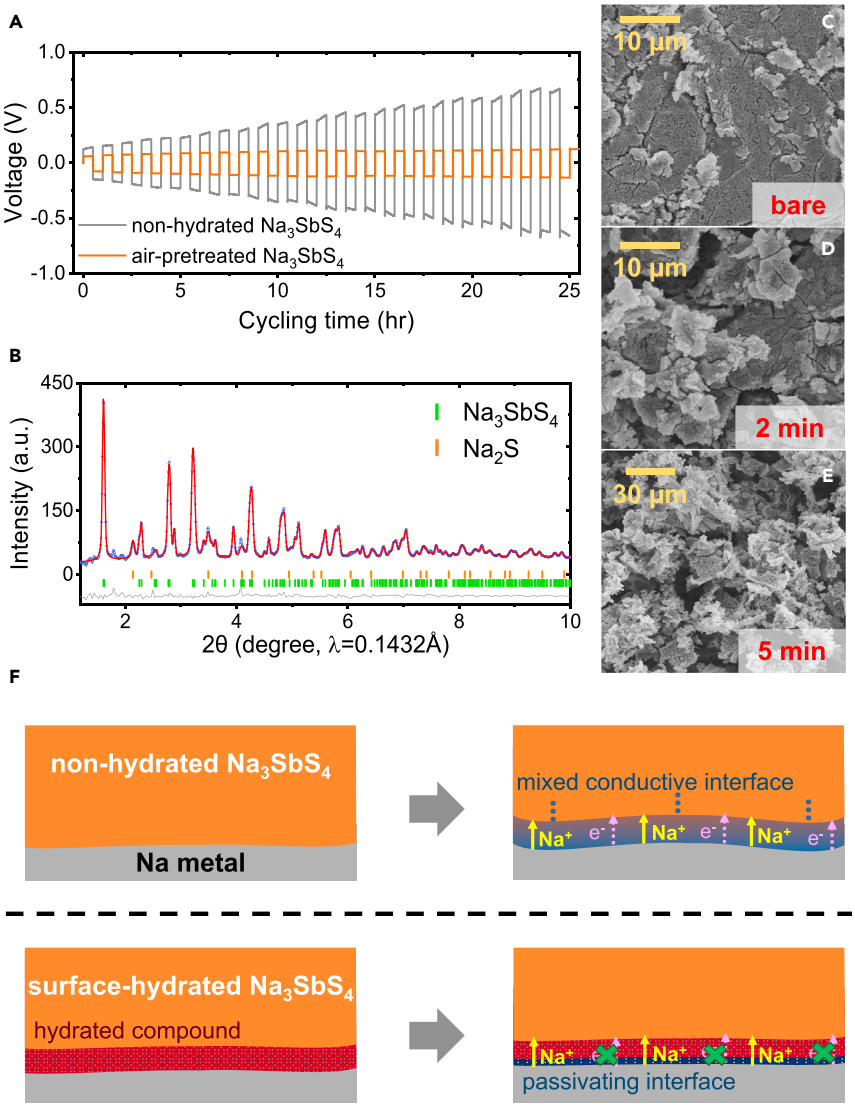

Figure 1. Enhancement of Na/Na_3SbS_4 Interfacial Stability via Surface Hydration of Solid-State Electrolyte

(A) Galvanostatic cycling of Na/Na_3SbS_4/Na symmetric cells with (orange) and without (gray) surface hydration pretreatment at a current density of 0.1 mA cm^{-2}.

(B) SXRD pattern and Rietveld refinement of Na_3SbS_4/Na interface products. The blue dots represent the observed intensities, and the red and dark gray curves represent the calculated intensities and the intensity difference between the observation and refinement fitting, respectively. The tick marks indicate the peak positions for Na_3SbS_4 (green) and Na_2S (orange).

(C–E) SEM images (and corresponding scale bars) of the surface of Na_3SbS_4 pellet after air exposure for different durations. (C) 0 min, bare. (D) 2 min, and (E) 5 min.

(F) Schematic illustration of solid electrolyte-Na metal interface before (left) and after (right) electrochemical cycling. A mixed conductive interface layer grew upon cycling of the non-hydrated Na_3SbS_4 (top), whereas a passivating interface was formed on the hydrated compound of the surface-hydrated Na_3SbS_4 (bottom).

Electrolyte Hydration Process and Discovery of $Na_3SbS_4 \cdot 8H_2O$

A strong correlation was observed between the (electro)chemical properties of the surface-hydrated Na_3SbS_4 and the air exposure time, with an optimal exposure time of 10 min (Figure 2A). For the cells using Na_3SbS_4 that were exposed to air for longer than 10 min, the voltage before cycling increased (shown as the gray

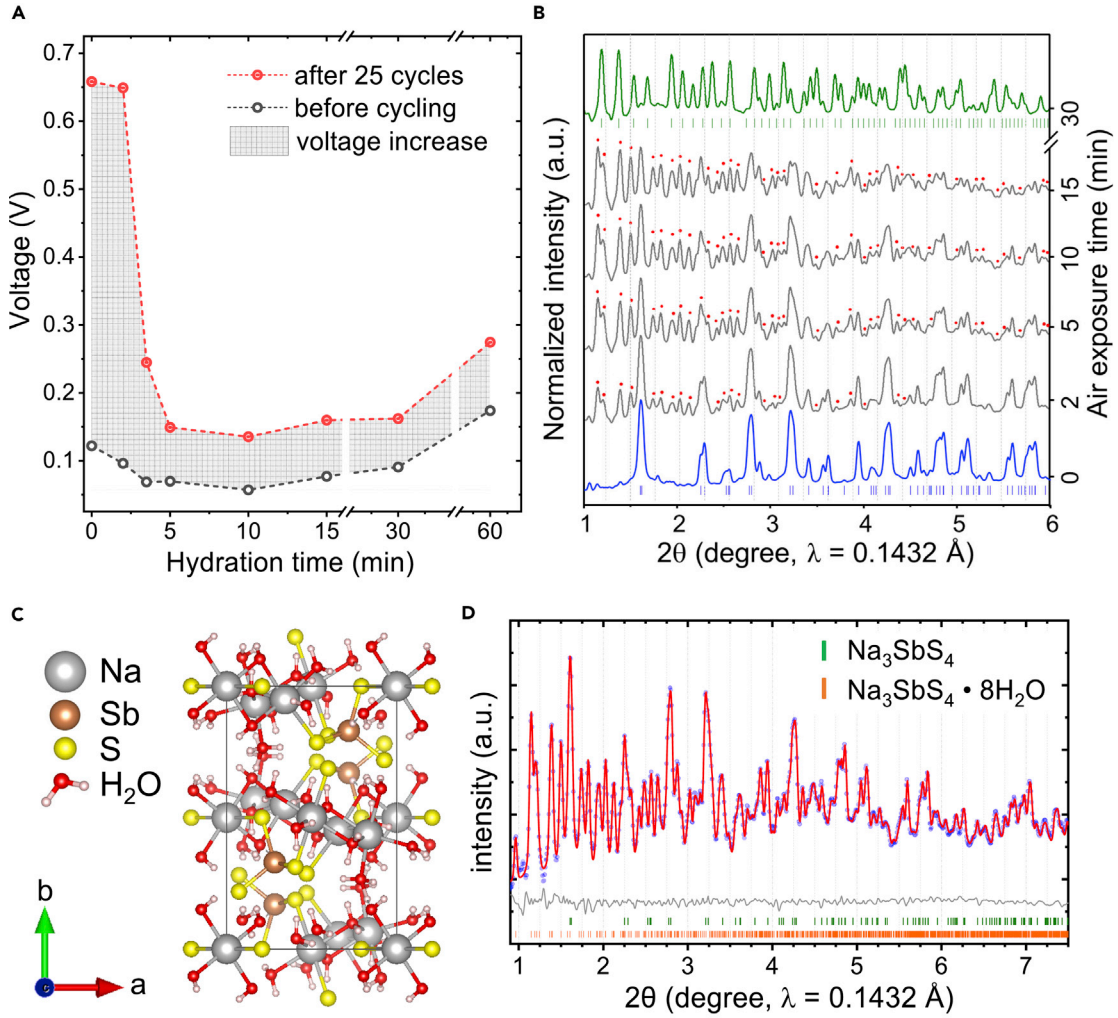

Figure 2. Hydration Process of Na_3SbS_4 and Discovery of $Na_3SbS_4 \cdot 8H_2O$

(A) Voltage of Na/Na_3SbS4/Na symmetric cells after different surface hydration pretreatment durations before (gray) and after (red) 25 cycles (0 min of surface pretreatment indicates the use of bare Na_3SbS_4 as the solid electrolyte). The grid-pattern-filled area represents the voltage increase of each symmetric cell upon cycling.

(B) SXRD patterns of Na_3SbS_4 after different durations of air exposure, with the tick marks indicating the peak positions for Na_3SbS_4 (blue) and $Na_3SbS_4 \cdot 9H_2O$ (green). The visible peaks corresponding to $Na_3SbS_4 \cdot 8H_2O$ are marked by dots.

(C) Crystal structure viewed along the [001] direction of $Na_3SbS_4 \cdot 8H_2O$.

(D) SXRD pattern and Rietveld refinement of Na_3SbS_4 after 10 min of air exposure. The blue dots represent the observed intensities, and the red and dark gray curves represent the calculated intensities and intensity difference between the observation and refinement fitting, respectively. The tick marks indicate the peak positions for Na_3SbS_4 (green) and $Na_3SbS_4 \cdot 8H_2O$ (orange).

dash line), suggesting an increase in the overall cell impedance. The voltage growth after 25 cycles (shown as the grid-pattern-filled area) in these cells was similar to that observed in the cell with 10 min of air exposure, indicating similar stability against Na metal. This finding motivated us to determine whether different phases were produced during the air exposure or whether this correlation between exposure time and electrochemical performance was simply because of the expected change in the interface morphology against exposure time (i.e., increase of thickness).

To monitor the phase transformation of Na_3SbS_4 during the hydration process in ambient air, SXRD patterns were collected from a Na_3SbS_4 powder sample over

Please cite this article in press as: Tian et al., Reactivity-Guided Interface Design in Na Metal Solid-State Batteries, Joule (2019), https://doi.org/10.1016/j.joule.2018.12.019

120 min of air exposure (Figure 2B). A new phase (the visible peaks marked by the red-colored dots) appears after 2 min of air exposure, together with Na_3SbS_4 (allowed peaks marked with blue-colored tick marks). Unexpectedly, the newly produced peaks do not correspond to those for the previously reported $Na_3SbS_4 \cdot 9H_2O$ phase. The fully hydrated phase $Na_3SbS_4 \cdot 9H_2O$ does not appear until approximately 30 min of air exposure. Because the hydration and dehydration of Na_3SbS_4 have been reported to be reversible,[19,33] the new phase formed during the hydration of Na_3SbS_4 is likely an intermediate hydrate phase containing less crystal water. The formation time of the intermediate hydrate phase corresponds to the optimal pretreatment time of the solid-state electrolyte, indicating that the improved cathodic stability of the surface-treated Na_3SbS_4 is due to the formation of this intermediate hydrate phase rather than the fully hydrated one.

We attempted to determine the composition and structure of this intermediate hydrate phase. *Ab initio* structure determination from powder diffraction data is challenging, which was further complicated by the presence of more than two phases and no prior knowledge of the phase composition, making the commonly employed structural solution approaches (e.g., simulated annealing, direct method) infeasible. Instead, we proposed structures by substituting atoms in all hydrated compounds associated with Na_3AX_4 (A = P, As, Sb; X = S, Se) that appeared in the Inorganic Crystal Structure Database (ICSD),[38] and these structures were then tested against the diffraction data using Rietveld refinements. The intermediate hydrate compound (Figure 2D) was identified as $Na_3SbS_4 \cdot 8H_2O$, which was obtained by substituting As for Sb and D for H in $Na_3AsS_4 \cdot 8D_2O$[39,40] as shown in Figure 2C. The structural parameters of the as-prepared $Na_3SbS_4 \cdot 8H_2O$ determined from the Rietveld refinement of the SXRD data are listed in Tables S3 and S4. A detailed structural description is provided in Note S1. Using density functional theory (DFT) calculations, the energy of the monoclinic ($P2_1/c$, No. 14) $Na_3SbS_4 \cdot 8H_2O$ structure was calculated to be only 11 meV/atom above the compositional convex hull, well within the range of energy where many synthesizable low-energy metastable compounds are found.[41] However, our efforts to isolate $Na_3SbS_4 \cdot 8H_2O$ as a single phase were unsuccessful.

To understand the Na-ion transport mechanisms in $Na_3SbS_4 \cdot 8H_2O$ and $Na_3SbS_4 \cdot 9H_2O$, we performed nudged elastic band (NEB) calculations of Na-vacancy migration barriers of both structures. The lowest migration barrier and the corresponding optimal minimum energy path (MEP) that percolates each structure are shown in Figure 3. The vacancy migration barrier of $Na_3SbS_4 \cdot 8H_2O$ is calculated to be 502 meV (Figure 3A) along the [100] direction, as shown in Figure 3B. This migration barrier is comparable to that of lithium phosphorus oxynitride (LiPON) reported in previous studies,[42,43] suggesting reasonable Na-ion conductivity of $Na_3SbS_4 \cdot 8H_2O$. Detailed descriptions of the Na-ion diffusion channels and transport mechanisms are presented in Note S1 and Figures S6 and S7. Similarly, the vacancy migration barrier of $Na_3SbS_4 \cdot 9H_2O$ is calculated to be 920 meV (Figure 3A) along the [010] direction, as shown in Figure 3C, which is consistent with previous reports of the low Na-ion conductivity of the structure.[44] The much higher migration barrier in $Na_3SbS_4 \cdot 9H_2O$ precludes any substantial Na mobility through it and indicates the importance of a relatively short hydration process to reach the $Na_3SbS_4 \cdot 8H_2O$ but not the $Na_3SbS_4 \cdot 9H_2O$ phase.

Interface Stabilization Mechanism and Characterization of Interface Products

Based on the findings discussed above, we can rationalize the complex interface chemistry by which the surface-hydrated Na_3SbS_4 improves the interfacial stability

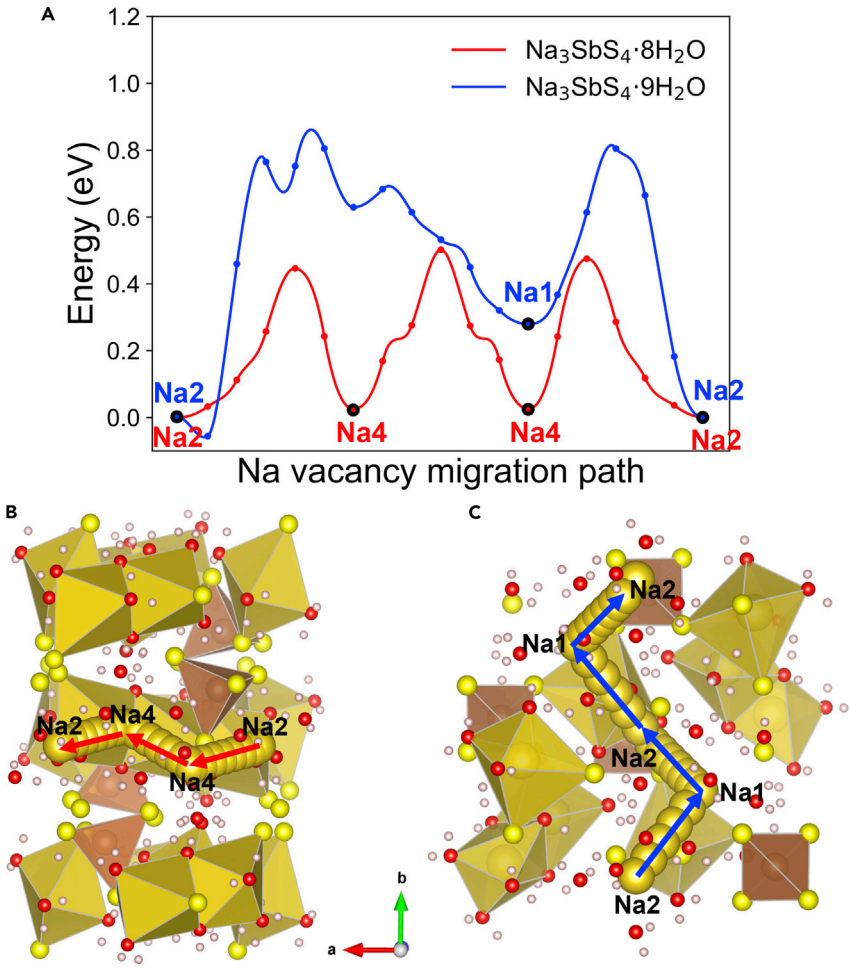

Figure 3. Na Vacancy Migration Energies and Transport Mechanism in $Na_3SbS_4 \cdot 8H_2O$ and $Na_3SbS_4 \cdot 9H_2O$

(A) Na vacancy migration energy along the minimum energy paths (MEPs).

(B and C) Na vacancy migration pathway with minimal percolation barrier in $Na_3SbS_4 \cdot 8H_2O$ along the [100] direction (B) and in $Na_3SbS_4 \cdot 9H_2O$ along the [010] direction (C). $Na(H_2O,S)_6$ octahedra and SbS_4 tetrahedra are colored in yellow and brown, respectively. The Na transport channel is represented by the hopping Na atoms (labeled consistently with Note S1) and the red or blue arrows.

against Na metal. Upon air exposure for an optimal duration, $Na_3SbS_4 \cdot 8H_2O$ is formed instead of the fully hydrated phase on the surface of Na_3SbS_4. The reaction between $Na_3SbS_4 \cdot 8H_2O$ and Na metal can be evaluated using DFT and is found to be similar to that of the fully hydrated phase, leading to the formation of the following interface:

$$40\ Na + Na_3SbS_4 \cdot 8H_2O \rightarrow 4\ Na_2S + Na_3Sb + 16\ NaH + 8\ Na_2O. \quad \text{(Reaction 3)}$$

The interfacial decomposition products were experimentally determined using a spatially resolved *post-operando* SXDP experiment. The experiment was performed on a symmetric Na/Na_3SbS_4/Na cell at beam line 11-ID-B at APS using the radially accessible tubular *in situ* X-ray (RATIX) cell adapted for X-ray transmission.[45] The cell was cycled at a constant current (0.1 mA cm^{-2}) for 25 h of the Na plating/stripping processes. The post-cycled cell was oriented vertically, with the X-ray beam

Please cite this article in press as: Tian et al., Reactivity-Guided Interface Design in Na Metal Solid-State Batteries, Joule (2019), https://doi.org/10.1016/j.joule.2018.12.019

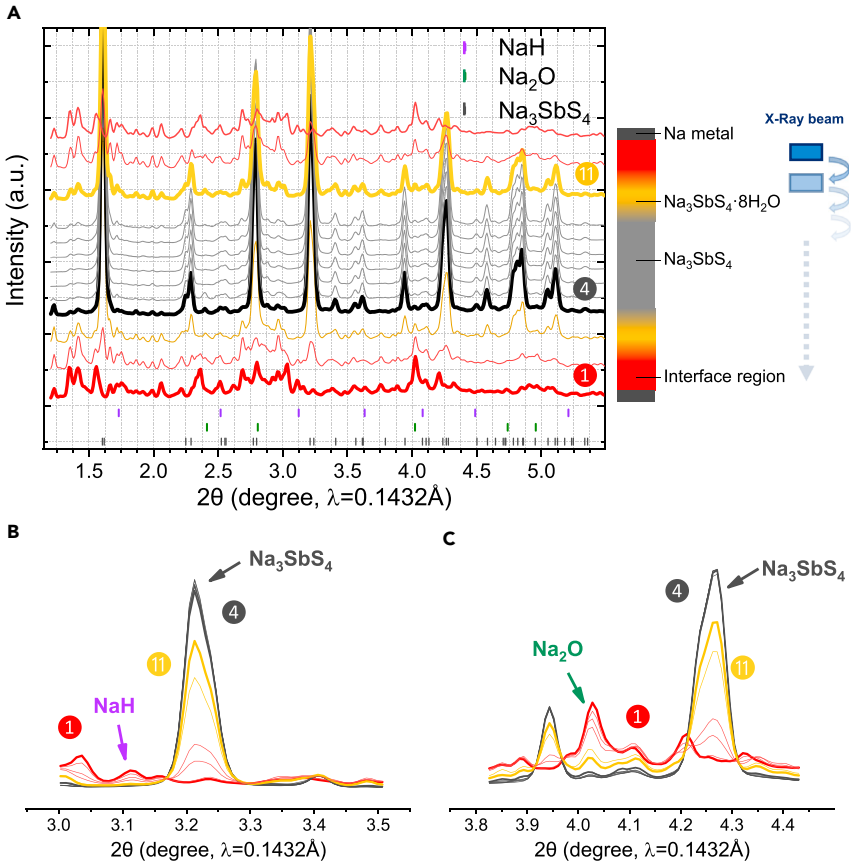

Figure 4. Spatially Resolved *Post-Operando* SXRD Profiles of Na/Na_3SbS_4/Na Symmetric Cell with Surface Hydrate Coating

(A) SXRD depth profiling of symmetric cell along the vertical axis of the cell. Each pattern corresponds to one layer of the schematic illustration on the right marked by multiple colors. The three bolded patterns mark the three region boundaries in the symmetric cell.

(B and C) Enlargement of XRD profiles from 3.0° to 3.5° (B) and 3.8° to 4.5° (C). Visible peaks for NaH, Na_2O, and Na_3SbS_4 are marked by arrows.

transmitted through the cell horizontally. To achieve better mapping resolution, the size of the beam was reduced to 50 μm in the vertical direction along the cell. Diffraction patterns were obtained consecutively at 13 positions between two current collectors. Details of the experimental setup are provided in the Experimental Procedures. Figure 4A displays SXRD patterns collected at different positions along the vertical direction of the Na/surface-hydrated Na_3SbS_4/Na symmetric cell. $Na_3SbS_4 \cdot 8H_2O$ is observed in three SXRD patterns next to Na metal (see the patterns colored in red and yellow in Figure 4A). All the Bragg reflections from the bulk solid-state electrolyte region can be indexed to Na_3SbS_4 (see the bolded pattern no. 4 colored in gray in Figure 4A), suggesting perfect sealing of the cell. Decomposition products, such as NaH and Na_2O, together with $Na_3SbS_4 \cdot 8H_2O$ were identified in the two layers closest to the Na metal (see the bolded pattern no. 1 colored in red in Figures 4A–4C, detailed Rietveld refinement shown in Figure S8). The third closest layer (see the bolded pattern no. 11 colored in yellow in Figure 4A) consisted of a two-phase mixture of $Na_3SbS_4 \cdot 8H_2O$ and Na_3SbS_4. The detection of NaH and Na_2O agrees well with our computational prediction for the reaction between Na metal and $Na_3SbS_4 \cdot 8H_2O$ in Reaction 3. The presence of Na

Please cite this article in press as: Tian et al., Reactivity-Guided Interface Design in Na Metal Solid-State Batteries, Joule (2019), https://doi.org/10.1016/j.joule.2018.12.019

metal was observed after the cell was disassembled. These results confirm the protection of Na metal by hydration of the electrolyte.

DISCUSSION

Most solid conductors are not stable against the strong reduction potential of alkali metal anodes and require the use of barrier layers or accidental passivation. The best passivation is one that is designed to give ionically conducting products from the reaction of the conductor with the alkali metal. This "built-in" passivation guarantees that even freshly generated interfaces are passivated, in contrast to externally applied barrier layers. In our example, we partially stabilized the interface between the sulfide conductor Na_3SbS_4 and Na metal by the formation of NaH and Na_2O through air exposure of the solid electrolyte pellet for a certain duration. The fast phase transformation between Na_3SbS_4, $Na_3SbS_4 \cdot 8H_2O$, and $Na_3SbS_4 \cdot 9H_2O$ in ambient air at room temperature suggests the fast reaction kinetics of water uptake and release, which may have led to the preferred generation of NaH and Na_2O over other products from the reduction of Sb when the hydrated compounds contacted Na metal. In fact, the stability between Na_3SbS_4 and Na metal might have been achieved accidentally without realizing the effect of hydrate protection. In contrast to other observations and theoretical predictions,[19,32,33] the interface between Na_3SbS_4 and Na metal was reported to be stable in one previous study[44] in which Na_3SbS_4 was synthesized by heating $Na_3SbS_4 \cdot 9H_2O$. The reported thermogravimetric analysis results during the dehydration process indicated the presence of residual crystal water, which may explain the observed compatibility.

Hydrates have broadened the material horizons of battery research,[46] in particular as protective layers for metal anodes. To broaden the impact of our work in metal-based solid-state batteries, we evaluated the reactions between all the unique Li/Na-containing hydrated compounds present in the Materials Project database[34] and Li/Na metal. All 32 of the unique Na-based hydrated compounds reacted with Na at 0 V (i.e., complete reduction) to form NaH, and 25 out of 32 reacted with Na to form Na_2O. In addition, all 37 of the unique Li-based hydrated compounds reacted with Li to form both LiH and Li_2O at 0 V. These predicted reactions are summarized in Tables S5 and S6. This suggests hydrates are promising materials for metal electrode protection in solid-state batteries, which, in certain cases, can be formed *in situ* simply through air exposure.

Furthermore, our work highlights the importance of reverse interface design. Rather than designing conductors for which reactivity with the electrodes is left to chance, reaction to passivating products should be designed from the start. Based on our high-throughput screening results on the decomposition products of multiple Na-ion conductors, we used hydrated compounds as a chemical initiator to beneficially react with the alkali metal to construct the designed interface. The reaction between the hydrated compound and metallic electrode introduces preferred passivating products at the interface (i.e., NaH and Na_2O, as demonstrated in this work) and reduces the fraction of electronically conducting phases (i.e., Na_3Sb) that cause continuous interface growth. Using the proposed general strategy of interface reverse design, pretreatment using other chemicals can be performed to regulate the metal-electrolyte interface. For example, Li_2S is another passivating product that can possibly be introduced in the interface. Gas processing of sulfide-based conductors using SO_2 can produce a sulfur-rich layer on the electrolyte surface (such as the generation of S or Li_4GeS_4 in Reaction 4 and Reaction 5 calculated by DFT), which may serve as initiators to introduce Li_2S at the metal-electrolyte interface.

Please cite this article in press as: Tian et al., Reactivity-Guided Interface Design in Na Metal Solid-State Batteries, Joule (2019), https://doi.org/10.1016/j.joule.2018.12.019

Interestingly, several gases[21,47] (N_2, O_2, CO_2, and SO_2) were considered for use as the pretreatment gas in an Li-metal liquid cell, and among these gases, SO_2 was determined to be the most effective gas for the construction of a thin passivation layer.

$$2\ SO_2\ +\ Li_3PS_4\ \rightarrow\ Li_3PO_4\ +\ 6\ S. \qquad \text{(Reaction 4)}$$

$$2\ SO_2\ +\ 0.5\ Li_{10}Ge(PS_6)_2\ \rightarrow\ Li_3PO_4\ +\ 0.5\ Li_4GeS_4\ +\ 6\ S. \qquad \text{(Reaction 5)}$$

Finally, together with the phase fraction of each interface component, the spatial distribution of different components is equally important in determining interface transport properties. Developing a rational strategy toward solid electrolyte interphase (SEI) morphology optimization in solid-state batteries has been hindered by the nanoscale thickness of this interfacial layer, which poses significant characterization challenges. *Ex situ* X-ray and/or neutron total scattering techniques can provide useful information about the interface decomposition products, but sample preparation requires physical separation of the interfacial layer followed by grinding it into a powder, which may lead to further reactions. Figure S9 compares the *ex situ* and *post-operando* SXRD patterns of the Na/$Na_3SbS_4{\cdot}8H_2O$ interface. $Na_3SbS_4{\cdot}8H_2O$, NaH, and Na_2O can be clearly identified at the interface in the *post-operando* SXRD pattern but are not detectable in the *ex situ* diffraction pattern because of the presence of excess Na_3SbS_4 from the bulk electrolyte and the generation of Na_2S from the further reaction of Na metal and Na_3SbS_4 during grinding. These results suggest that non-destructive methods such as *in situ* depth-profiling experiments can provide more accurate information about the composition and spatial distribution of interfacial reaction products than *ex situ* experiments. We believe that future work using *in situ* depth-profiling experiments and tomography techniques will deepen our understanding of the morphological evolution of the interface,[48–50] which is crucial for solid-state battery research.

Conclusions

Herein, an effective strategy for the reverse design of the metal/electrolyte interface in solid-state batteries based on first-principles calculations of passivating reaction products was presented. Using this strategy, the strongly reacting interface between Na_3SbS_4 and Na metal was partially stabilized via electrolyte hydration achieved by exposing the electrolyte pellet to ambient air. This rapid and simple air treatment greatly improved the stability of the Na_3SbS_4 electrolyte-Na metal interface upon electrochemical cycling. The formation of a newly discovered hydrate phase, $Na_3SbS_4{\cdot}8H_2O$, led to the generation of desired passivating products (i.e., NaH and Na_2O) at the interface, which suppressed the electrolyte decomposition. The spatially resolved multilayered phase distribution in the Na metal symmetric cell was characterized using non-destructive *post-operando* SXDP, providing valuable information about the metal-electrolyte interface that was consistent with our theoretical predictions. Our work identifies hydrates as a promising class of materials for stabilization of the metal-electrolyte interface of solid-state batteries, together with the interface reverse design strategy, providing a new path for the discovery of a wide range of other potential passivating products.

EXPERIMENTAL PROCEDURES

Na_3SbS_4 was synthesized using a solid-state sintering method. Na_2S (Alfa Aesar, 99.8%), antimony (Sigma-Aldrich, 99.5% trace metals basis), and sulfur (Sigma-Aldrich, $\geq$99.5%) were used as precursors. A stoichiometric amount of powder precursors was mixed in an argon-filled glovebox. The resulting mixture (~1 g) was then placed into a boron nitride tube (3-mm inner diameter and 4-mm outer diameter),

Please cite this article in press as: Tian et al., Reactivity-Guided Interface Design in Na Metal Solid-State Batteries, Joule (2019), https://doi.org/10.1016/j.joule.2018.12.019

which was wrapped in aluminum foil, with the open end sealed with a stainless-steel Swagelok cap (9.525 mm). This tube was transferred into a sealed alumina tube furnace, which was purged with pre-dried Ar gas (oxygen/moisture traps, model MT200-4-D, Agilent). The temperature of the furnace was rapidly increased to 550°C within ~30 min and then held for 17 h to allow the reaction to complete. During the reaction, a continuous flow of Ar gas with a flow rate of approximately 50 mL min^{-1} was used. The resulting products were collected after the furnace was naturally cooled to room temperature and then immediately transferred into the glovebox and manually ground into powder.

The Na-ion conductivity of Na_3SbS_4 was evaluated using electrochemical impedance spectroscopy (EIS) with tantalum electrodes at temperatures ranging from 25°C to 80°C. The as-prepared Na_3SbS_4 powder was uniaxially compressed under a pressure of approximately 350 MPa before being sandwiched by tantalum foils (~0.05-mm thick) (Sigma-Aldrich, ≥99.9%), which corresponds to an applied pressure of approximately 520 MPa. The ionic conductivities were measured for a 2.33-mm-thick pellet with a diameter of 6 mm. EIS measurements were performed using an EC-Lab Electrochemistry SP300, Biologic. The measurements were conducted at the initial open-circuit voltage in the frequency range of 7 MHz to 10 mHz with the application of a 10-mV signal amplitude. The measurements were performed using a Biologic Controlled Environment Sample Holder assembled and sealed in an Ar-filled glovebox.

To prepare the Na metal symmetric cells, ~140 mg of Na_3SbS_4 powder was cold pressed into a pellet under a pressure of ~350MPa for 5 min within an in-house-designed pressure cell (7.7-mm inner diameter) in an Ar-filled glovebox. For the electrolyte hydration treatment, the resulting Na_3SbS_4 pellet (~1-mm thick) was exposed to ambient air (humidity ~68%) to coat the Na_3SbS_4 pellet. Two metallic Na foils (6-mm diameter and <50-μm thick) were then carefully attached on both sides of the pellet. The cells were assembled under an Ar atmosphere with otherwise identical procedures, and Na_3SbS_4 from the same batch of sintered powder was used to maximize consistency. EIS measurements of the samples were performed at room temperature (~25°C) immediately after cell assembly. The symmetric cells were then cycled with a constant current density of 0.1 mA cm^{-2} at room temperature for 25 h using an EC-Lab Electrochemistry VMP300, Biologic. During cycling, the current direction was reversed every 30 min. A constant spring pressure (~3 MPa) was applied within the pressure cells during cycling. SEM images were obtained on a Zeiss Gemini Ultra-55 analytical field-emission scanning electron microscope at the Molecular Foundry at Lawrence Berkeley National Laboratory (LBNL).

To observe the phase transformation process of Na_3SbS_4 upon air exposure, the as-prepared Na_3SbS_4 powder was exposed to ambient air (humidity ~68%) under continuous grinding with a mortar and pestle for specific air-exposure durations (0–120 min). The final products were collected and then packed and sealed into a 1.1049-mm diameter Kapton capillary for further characterization in an Ar-filled glovebox. SXRD experiments were performed at beamline 11-ID-B at the Advanced Photon Source (APS) of Argonne National Laboratory using a constant wavelength of 0.1432 Å. The use of high-energy X-rays (E = 86.57 keV) minimizes absorption effects. The Rietveld refinements were performed using the TOPAS 5.0 software package (Bruker).

For phase determination of the products at the Na/solid electrolyte interface, spatially resolved *post-operando* XRD patterns of the symmetric cells were collected at beamline 11-ID-B at APS using the RATIX cell[45] adapted for X-ray transmission.

The cells were prepared in an Ar atmosphere using the same materials as those used for the pressure cell measurements and were well sealed to eliminate the safety concern related to Na metal or NaH. The post-cycled RATIX cell was oriented perpendicularly to the X-ray beam (λ = 0.1432 Å). The width of the beam was 50 μm along the direction of the cell. The detector was positioned at a distance of 95 cm from the sample. The acquisition time for each diffraction pattern was 1 s, and the diffraction patterns were obtained consecutively at 13 positions from top to bottom along the vertical direction of the cell. Background measurements were collected using identical cells but without the testing materials present. A CeO_2 standard was used to determine the sample geometry and sample-to-detector distance. The data were integrated into a function of intensity versus 2θ using FIT2D.[51] Standard corrections (background, Compton scattering, and detector effects) were applied, and Rietveld refinements were performed using the TOPAS 5.0 software package (Bruker).

The interface reactivity was investigated with previously published methods,[22,25] which evaluate the driving force for possible products to form. We believe that such a thermodynamics-based approach provides a better approximation of the experimental condition than trying to observe interfacial reactions from direct DFT structural relaxation. DFT calculation for the total energy of $Na_3SbS_4 \cdot 8H_2O$ structure uses the Perdew-Burke-Ernzerhof (PBE) generalized gradient approximations[52] as implemented in the Vienna Ab initio Simulation Package (VASP).[53] The interactions between ion cores and valence electrons are described by projector augmented wave (PAW) method.[54] A plane-wave energy cutoff of 520 eV and a k-point density of at least $1,000/n_{atom}$ are used. Energy above the compositional convex hull for $Na_3SbS_4 \cdot 8H_2O$ is evaluated by constructing a convex hull with pre-computed DFT energies for materials in the same chemical space from Materials Project database[34] using the Pymatgen software package.[55] Reaction products at 0 V versus Na metal are calculated using the same DFT energy dataset following the method employed in our previous work.[25]

To study the Na-ion diffusion in $Na_3SbS_4 \cdot 8H_2O$ and $Na_3SbS_4 \cdot 9H_2O$, we performed climbing-image nudged elastic band (NEB) calculations[56,57] to determine the vacancy migration mechanism using DFT-calculated energies and forces. The vacancy was created by removing one Na ion from the pristine structure. Supercells containing 8 formula units were used for $Na_3SbS_4 \cdot 8H_2O$ and $Na_3SbS_4 \cdot 9H_2O$ to minimize the interaction between periodic images. A 2 × 1 × 1 k-point grid was used, and the plane-wave energy cutoff was set to 400 meV for the NEB calculations.

SUPPLEMENTAL INFORMATION

Supplemental Information includes nine figures, six tables, one note, and one data file and can be found with this article online at https://doi.org/10.1016/j.joule.2018.12.019.

ACKNOWLEDGMENTS

This work was supported by the Samsung Advanced Institute of Technology. D.C.H. was supported as part of the Joint Center for Energy Storage Research (JCESR), an Energy Innovation Hub funded by the U.S. Department of Energy, Office of Science, and Basic Energy Sciences, subcontract 3F-31144. This research used resources of the Advanced Photon Source, a U.S. Department of Energy (DOE) Office of Science User Facility operated for the DOE Office of Science by Argonne National Laboratory under Contract No. DE-AC02-06CH11357. Synchrotron XRD data were

collected at the X-ray Science Division Beamline 11 ID-B at the Advanced Photon Source, Argonne National Laboratory. The SEM experiments were performed at the Molecular Foundry, LBNL, supported by the Office of Science, Office of Basic Energy Sciences of the US Department of Energy (Contract No. DE-AC02-05CH11231). The authors thank Dr. Valentina Lacivita, Dr. Penghao Xiao, Dr. Jaechul Kim, Dr. Pieremanuele Canepa, Dr. Huiwen Ji, and Dr. Deok-Hwang Kwon for valuable discussions and Dr. Olaf Borkiewicz and Dr. Kevin Beyer for their assistance at APS.

AUTHOR CONTRIBUTIONS

Y.T., S.-H.B., and G.C. designed the study. Y.T. and Y.S. performed the solid-state synthesis and electrochemistry characterization; Y.T., H.L., and K.W.C. conducted the synchrotron X-ray diffraction measurements; Y.T. and S.-H.B. performed the structure analysis; Y.S. conducted the impedance characterization; and D.C.H. and Y.X. performed the first-principles calculations. Y.T., Y.S., D.C.H., Y.X., and S.-H.B. jointly performed all the data analysis and wrote the manuscript together with G.C. All the authors approved the final version of the manuscript.

DECLARATION OF INTERESTS

The authors declare no competing interests. A patent related to this work is submitted.

Received: September 19, 2018
Revised: November 14, 2018
Accepted: December 18, 2018
Published: January 23, 2019

REFERENCES

1. Janek, J., and Zeier, W.G. (2016). A solid future for battery development. Nat. Energy *1*, 16141.
2. Li, J., Ma, C., Chi, M., Liang, C., and Dudney, N.J. (2015). Solid electrolyte: the key for high-voltage lithium batteries. Adv. Energy Mater *5*, 1401408.
3. Ihlefeld, J.F., Clem, P.G., Doyle, B.L., Kotula, P.G., Fenton, K.R., and Apblett, C.A. (2011). Fast lithium-ion conducting thin-film electrolytes integrated directly on flexible substrates for high-power solid-state batteries. Adv. Mater. *23*, 5663–5667.
4. Noguchi, Y., Kobayashi, E., Plashnitsa, L.S., Okada, S., and Yamaki, J. (2013). Fabrication and performances of all solid-state symmetric sodium battery based on NASICON-related compounds. Electrochim. Acta *101*, 59–65.
5. Jian, Z., Hu, Y.S., Ji, X., and Chen, W. (2017). NASICON-structured materials for energy storage. Adv. Mater. *29*, 201601925.
6. Feng, J.K., Yan, B.G., Liu, J.C., Lai, M.O., and Li, L. (2013). All solid state lithium ion rechargeable batteries using NASICON structured electrolyte. Mater. Technol. *28*, 276–279.
7. Thangadurai, V., Narayanan, S., and Pinzaru, D. (2014). Garnet-type solid-state fast Li ion conductors for Li batteries: critical review. Chem. Soc. Rev. *43*, 4714–4727.
8. Han, X., Gong, Y., Fu, K.K., He, X., Hitz, G.T., Dai, J., Pearse, A., Liu, B., Wang, H., Rubloff, G., et al. (2017). Negating interfacial impedance in garnet-based solid-state Li metal batteries. Nat. Mater. *16*, 572–579.
9. Buschmann, H., Dölle, J., Berendts, S., Kuhn, A., Bottke, P., Wilkening, M., Heitjans, P., Senyshyn, A., Ehrenberg, H., Lotnyk, A., et al. (2011). Structure and dynamics of the fast lithium ion conductor "$Li_7La_3Zr_2O_{12}$". Phys. Chem. Chem. Phys. *13*, 19378–19392.
10. Murayama, M., Sonoyama, N., Yamada, A., and Kanno, R. (2004). Material design of new lithium ionic conductor, thio-LISICON, in the Li_2S–P_2S_5 system. Solid State Ion *170*, 173–180.
11. Seino, Y., Nakagawa, M., Senga, M., Higuchi, H., Takada, K., and Sasaki, T. (2015). Analysis of the structure and degree of crystallisation of $70Li_2S$-$30P_2S_5$ glass ceramic. J. Mater. Chem. A *3*, 2756–2761.
12. Kamaya, N., Homma, K., Yamakawa, Y., Hirayama, M., Kanno, R., Yonemura, M., Kamiyama, T., Kato, Y., Hama, S., Kawamoto, K., et al. (2011). A lithium superionic conductor. Nat. Mater. *10*, 682–686.
13. Trevey, J.E., Jung, Y.S., and Lee, S.H. (2011). High lithium ion conducting Li_2S-GeS_2-P_2S_5 glass-ceramic solid electrolyte with sulfur additive for all solid-state lithium secondary batteries. Electrochim. Acta *56*, 4243–4247.
14. Seino, Y., Ota, T., Takada, K., Hayashi, A., and Tatsumisago, M. (2014). A sulphide lithium super ion conductor is superior to liquid ion conductors for use in rechargeable batteries. Energ. Environ. Sci. *7*, 627–631.
15. Richards, W.D., Wang, Y., Miara, L.J., Kim, J.C., and Ceder, G. (2016). Design of $Li_{1+2x}Zn_{1-x}PS_4$, a new lithium ion conductor. Energy Environ. Sci. *9*, 3272–3278.
16. Wang, Y., Richards, W.D., Bo, S.-H., Miara, L.J., and Ceder, G. (2017). Computational prediction and evaluation of solid-state sodium superionic conductors $Na_7P_3X_{11}$ (X = O, S, Se). Chem. Mater. *29*, 7475–7482.
17. Bo, S.H., Wang, Y., Kim, J.C., Richards, W.D., and Ceder, G. (2016). Computational and experimental investigations of Na-Ion conduction in cubic Na_3PSe_4. Chem. Mater. *28*, 252–258.
18. Bo, S.H., Wang, Y., and Ceder, G. (2016). Structural and Na-ion conduction characteristics of $Na_3PS_xSe_{4-x}$. J. Mater. Chem. A *4*, 9044–9053.
19. Banerjee, A., Park, K.H., Heo, J.W., Nam, Y.J., Moon, C.K., Oh, S.M., Hong, S.T., and Jung, Y.S. (2016). Na_3SbS_4: a solution processable sodium superionic conductor for all-solid-state sodium-ion batteries. Angew. Chem. *55*, 9786–9790.
20. Wang, Y., Richards, W.D., Ong, S.P., Miara, L.J., Kim, J.C., Mo, Y., and Ceder, G. (2015). Design principles for solid-state lithium superionic conductors. Nat. Mater. *14*, 1026–1031.

21. Cheng, X.B., Zhang, R., Zhao, C.Z., and Zhang, Q. (2017). Toward safe lithium metal anode in rechargeable batteries: a review. Chem. Rev. *117*, 10403–10473.

22. Tian, Y.S., Shi, T., Richards, W.D., Li, J.C., Kim, J.C., Bo, S.H., and Ceder, G. (2017). Compatibility issues between electrodes and electrolytes in solid-state batteries. Energy Environ. Sci. *10*, 1150–1166.

23. Han, F.D., Zhu, Y.Z., He, X.F., Mo, Y.F., and Wang, C.S. (2016). Electrochemical stability of $Li_{10}GeP_2S_{12}$ and $Li_7La_3Zr_2O_{12}$ solid electrolytes. Adv. Energy Mater. *6*, 1501590.

24. Wenzel, S., Leichtweiss, T., Weber, D.A., Sann, J., Zeier, W.G., and Janek, J. (2016). Interfacial reactivity benchmarking of the sodium ion conductors Na_3PS_4 and sodium β-alumina for protected sodium metal anodes and sodium all-solid-state batteries. ACS Appl. Mater. Interfaces *8*, 28216–28224.

25. Richards, W.D., Miara, L.J., Wang, Y., Kim, J.C., and Ceder, G. (2016). Interface stability in solid-state batteries. Chem. Mater. *28*, 266–273.

26. Zhu, Y., He, X., and Mo, Y. (2015). Origin of outstanding stability in the lithium solid electrolyte materials: insights from thermodynamic analyses based on first-principles calculations. ACS Appl. Mater. Interfaces *7*, 23685–23693.

27. Wenzel, S., Randau, S., Leichtweiß, T., Weber, D.A., Sann, J., Zeier, W.G., and Janek, J. (2016). Direct observation of the interfacial instability of the fast ionic conductor $Li_{10}GeP_2S_{12}$ at the lithium metal anode. Chem. Mater. *28*, 2400–2407.

28. Wang, C., Gong, Y., Liu, B., Fu, K., Yao, Y., Hitz, E., Li, Y., Dai, J., Xu, S., Luo, W., et al. (2017). Conformal, nanoscale ZnO surface modification of garnet-based solid-state electrolyte for lithium metal anodes. Nano Lett. *17*, 565–571.

29. Tikekar, M.D., Choudhury, S., Tu, Z.Y., and Archer, L.A. (2016). Design principles for electrolytes and interfaces for stable lithium-metal batteries. Nat. Energy *1*, 16114.

30. Liang, X., Pang, Q., Kochetkov, I.R., Sempere, M.S., Huang, H., Sun, X.Q., and Nazar, L.F. (2017). A facile surface chemistry route to a stabilized lithium metal anode. Nat. Energy *2*, 17119.

31. Lu, Y., Li, L., Zhang, Q., Niu, Z., and Chen, J.J.J. (2018). Electrolyte and interface engineering for solid-state sodium batteries. Joule *2*, 1747–1770.

32. Wu, E.A., Kompella, C.S., Zhu, Z., Lee, J.Z., Lee, S.C., Chu, I.H., Nguyen, H., Ong, S.P., Banerjee, A., and Meng, Y.S. (2018). New insights into the interphase between the Na metal anode and sulfide solid-state electrolytes: a joint experimental and computational study. ACS Appl. Mater. Interfaces *10*, 10076–10086.

33. Zhang, L., Zhang, D., Yang, K., Yan, X., Wang, L., Mi, J., Xu, B., and Li, Y. (2016). Vacancy-contained tetragonal Na_3SbS_4 superionic conductor. Adv. Sci. *3*, 1600089.

34. Jain, A., Ong, S.P., Hautier, G., Chen, W., Richards, W.D., Dacek, S., Cholia, S., Gunter, D., Skinner, D., Ceder, G., et al. (2013). Commentary: The Materials Project: a materials genome approach to accelerating materials innovation. APL Mater *1*, 4812323.

35. Wang, J.W., Liu, X.H., Mao, S.X., and Huang, J.Y. (2012). Microstructural evolution of tin nanoparticles during in situ sodium insertion and extraction. Nano Lett. *12*, 5897–5902.

36. Hao, S.Q., and Sholl, D.S. (2010). Role of Schottky defects in hydrogen and metal diffusion in NaH, MgH_2, and $NaMgH_3$. J. Phys. Chem. Lett. *1*, 2968–2973.

37. He, K., Lin, F., Zhu, Y., Yu, X., Li, J., Lin, R., Nordlund, D., Weng, T.C., Richards, R.M., Yang, X.Q., et al. (2015). Sodiation kinetics of metal oxide conversion electrodes: A Comparative Study with lithiation. Nano Lett. *15*, 5755–5763.

38. Hellenbrandt, M. (2004). The Inorganic Crystal Structure Database (ICSD)—present and future. Crystallogr. Rev. *10*, 17–22.

39. Dittmar, G., and Schafer, H. (1978). Crystal-structure of $Na_3AsS_4 \cdot 8H_2O$. Z. Naturforsch. B Chem. Sci. *33*, 678–681.

40. Mereiter, K., Preisinger, A., Baumgartner, O., Heger, G., Mikenda, W., and Steidl, H. (1982). Hydrogen-bonds in $Na_3AsS_4 \cdot 8D_2O$: Neutron-diffraction, X-ray-diffraction and vibrational spectroscopic studies. Acta Cryst. *38*, 401–408.

41. Sun, W., Dacek, S.T., Ong, S.P., Hautier, G., Jain, A., Richards, W.D., Gamst, A.C., Persson, K.A., and Ceder, G. (2016). The thermodynamic scale of inorganic crystalline metastability. Sci. Adv. *2*, e1600225.

42. Yu, X.H., Bates, J.B., Jellison, G.E., and Hart, F.X. (1997). A stable thin-film lithium electrolyte: Lithium phosphorus oxynitride. J. Electrochem. Soc. *144*, 524–532.

43. Zhao, S.L., Fu, Z.W., and Qin, Q.Z. (2002). A solid-state electrolyte lithium phosphorus oxynitride film prepared by pulsed laser deposition. Thin Solid Films *415*, 108–113.

44. Wang, H., Chen, Y., Hood, Z.D., Sahu, G., Pandian, A.S., Keum, J.K., An, K., and Liang, C. (2016). An air-stable Na_3SbS_4 superionic conductor prepared by a rapid and economic synthetic procedure. Angew. Chem. Int. Ed. *55*, 8551–8555.

45. Liu, H., Allan, P.K., Borkiewicz, O.J., Kurtz, C., Grey, C.P., Chapman, K.W., and Chupas, P.J. (2016). A radially accessible tubular in situ X-ray cell for spatially resolved operando scattering and spectroscopic studies of electrochemical energy storage devices. J. Appl. Crystallogr. *49*, 1665–1673.

46. Yamada, Y., Usui, K., Sodeyama, K., Ko, S., Tateyama, Y., and Yamada, A. (2016). Hydrate-melt electrolytes for high-energy-density aqueous batteries. Nat. Energy *1*, 16129.

47. Koch, S.L., Morgan, B.J., Passerini, S., and Teobaldi, G. (2015). Density functional theory screening of gas-treatment strategies for stabilization of high energy-density lithium metal anodes. J. Power Sources *296*, 150–161.

48. Seitzman, N., Johnston, S., Platt, H.A., Harvey, S., Son, S.-B., Zenyuk, I.V., Al-Jassim, M., and Pylypenko, S. (2017). X-ray tomography and thermography investigation of a high-modulus solid electrolyte for all solid-state batteries. ECS Meeting Abstracts *2017*, 2051.

49. Wang, S., Xu, H., Li, W., Dolocan, A., and Manthiram, A. (2018). Interfacial chemistry in solid-state batteries: Formation of interphase and its consequences. J. Am. Chem. Soc. *140*, 250–257.

50. Meng, J., Guo, H., Niu, C., Zhao, Y., Xu, L., Li, Q., and Mai, L.J.J. (2017). Advances in structure and property optimizations of battery electrode materials. Joule *1*, 1–26.

51. Hammersley, A. (1997). FIT2D: an introduction and overview. http://www.esrf.eu/computing/scientific/FIT2D/FIT2D_INTRO/fit2d.html.

52. Perdew, J.P., Burke, K., and Ernzerhof, M.J.P.R.L. (1996). Generalized gradient approximation made simple. Phys. Rev. Lett. *77*, 3865–3868.

53. Kresse, G., and Furthmüller, J.J.P.R.B. (1996). Efficient iterative schemes for ab initio total-energy calculations using a plane-wave basis set. Phys. Rev. B Condens. Matter. *54*, 11169–11186.

54. Blöchl, P.E.J.P.R. (1994). Projector augmented-wave method. Phys. Rev. B *50*, 17953–17979.

55. Ong, S.P., Richards, W.D., Jain, A., Hautier, G., Kocher, M., Cholia, S., Gunter, D., Chevrier, V.L., Persson, K.A., and Ceder, G. (2013). Python Materials Genomics (pymatgen): a robust, open-source python library for materials analysis. Comput. Mater. Sci. *68*, 314–319.

56. Jónsson, H., Mills, G., and Jacobsen, K.W. (1998). Nudged elastic band method for finding minimum energy paths of transitions. In Classical and Quantum Dynamics in Condensed Phase Simulations (World Scientific), pp. 385–404.

57. Henkelman, G., Uberuaga, B.P., and Jónsson, H. (2000). A climbing image nudged elastic band method for finding saddle points and minimum energy paths. J. Chem. Phys. *113*, 9901–9904.